ACS APPLIED MATERIALS & INTERFACES

www.acsami.org

Research Article

Understanding Hole Extraction of Inverted Perovskite Solar Cells

Zhewei Zhang, Madhu Sheri, Zachariah A. Page, Todd Emrick,* Akinori Saeki,* Yao Liu,* and Thomas P. Russell*

Cite This: *ACS Appl. Mater. Interfaces* 2020, 12, 56068−56075

Read Online

ACCESS | Metrics & More | Article Recommendations | Supporting Information

ABSTRACT: This paper describes a correlation between charge extraction and energy-level alignment at the interface of polymeric hole transport layers and perovskite active layers. By tailoring the composition of the conjugated backbone of the hole transport material, energy levels between perovskites and hole transport layers are varied. Matching the band alignment at perovskite/hole transport interfaces dramatically improved charge extraction and thus device performance. Time-resolved microwave conductivity measurements, performed to elucidate hole transfer kinetics, suggest that hole transport layer energy levels greatly influence hole extraction efficiency at this interface, a finding that agrees well with device performance metrics. Furthermore, photoluminescence, Mott−Schottky, and space charge limited current measurements support that energy-level alignment between the hole transport layer and perovskite active layer enables more efficient hole extraction and transport at the device interface. The insight surrounding hole extraction in inverted perovskite devices will help design effective hole transport materials, which, in turn, facilitates the production of more efficient solar cells.

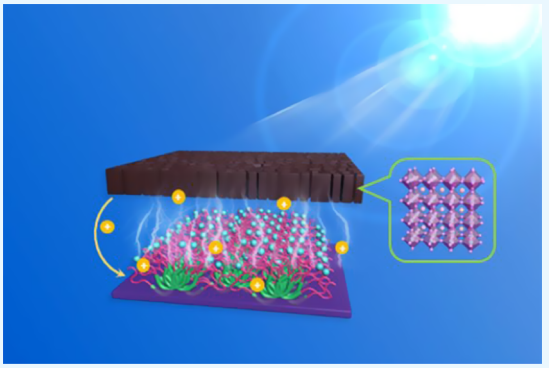

KEYWORDS: *perovskite solar cells, conjugated polymer, energy-level alignment, time-resolved microwave conductivity, hole transfer process*

INTRODUCTION

Perovskite solar cells (PSCs) are rapidly advancing the pace of photovoltaic research, with power conversion efficiencies (PCEs) increasing from 3.8% to a certified value of 25.2% over the last decade. The device structure of PSCs has evolved from liquid-based dye-sensitized solar cells to mesoporous structures with a solid hole transporter and to the planar heterojunction designs examined today.[1−5] Planar PSCs consist of a perovskite active layer sandwiched between solid charge transport layers, specifically a hole transport layer (HTL) and an electron transport layer (ETL). When an HTL is used as the device bottom contact, it defines an inverted configuration. Inverted PSCs, inspired by organic solar cells, have been of considerable interest since the discovery of bipolar transport in perovskites and perovskite/fullerene planar heterojunction in 2013.[6] In general, inverted PSCs are less efficient than their mesoscopic counterparts, but their fabrication is more straightforward and compatible with the well-established, solution-based, low-temperature roll-to-roll preparation used to produce organic solar cells.[7−9]

To achieve high-performance inverted PSC devices, efficient charge extraction and transport across each interface is critically important.[10,11] Optimal energy-level alignment for each of the contacting layers in the device will increase open-circuit voltage (V_{OC}) and enhance charge transport and extraction, thereby promoting a higher short-circuit current density (J_{SC}) and fill factor (FF).[12] The interfacial contact between the perovskite active layer and the HTL or ETL dictates charge extraction efficiency and, in turn, perovskite solar cell performance.[13−17] Fullerene and its derivatives, such as [6,6]-phenyl-C_{61}-butyric acid methyl ester ($PC_{61}BM$), are the most widely used ETL materials in inverted PSCs.[18] Fullerenes efficiently passivate trap states in perovskites, extract electrons, and block holes, making them highly successful ETL materials in inverted PSCs.[19−22] Poly(3,4-ethylenedioxythiophene):poly(styrenesulfonate) (PEDOT:PSS) was the first material examined as an HTL in inverted PSCs;[23] since then, numerous inorganic compounds,[24] such as NiO_x,[25−27] CuSCN,[28,29] PbS,[30] Cu_2O, and CuO,[31−33] have been tested as HTLs in PSCs. Recently, poly[bis(4-phenyl)(2,4,6-trimethylphenyl)amine] (PTAA) has been utilized as an effective HTL in inverted PSCs, yielding a PCE of 22.3%.[34] Nevertheless, a comprehensive understanding of hole extraction in inverted PSCs is still lacking. Notably, modulating the energy level of the HTL is advantageous for improving band alignment and charge extraction at the perovskite/HTL interface in inverted PSCs.[35−37] For example, surface modification of PEDOT:PSS increases the work

Received: October 8, 2020
Accepted: November 23, 2020
Published: December 7, 2020

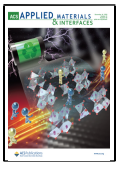

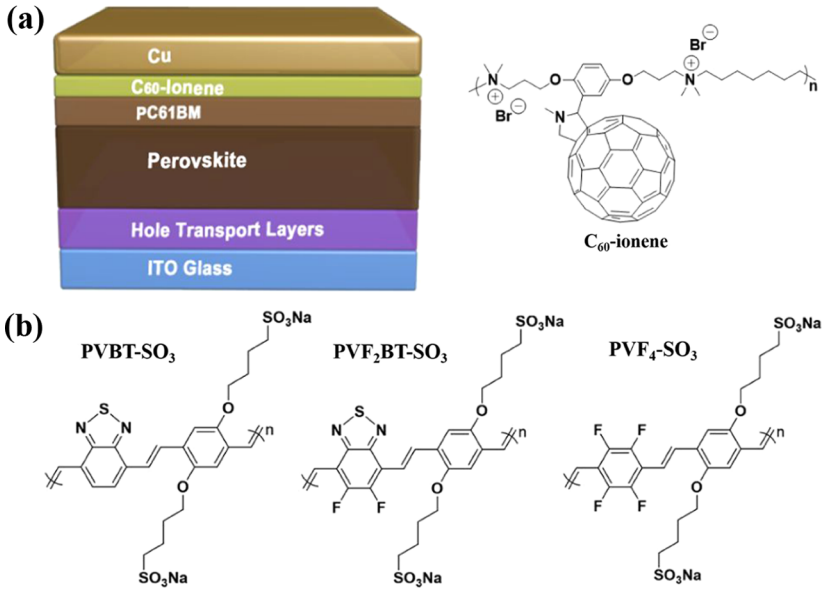

Figure 1. (a) Schematic of the device architecture: ITO/HTL/$MAPbI_3$/$PC_{61}BM$/C_{60}-Ionene/Cu; (b) chemical structures of the polymeric HTLs; and (c) chemical structure of C_{60}-ionene.

function and correspondingly the V_{OC} of perovskite devices.[38] In general, organic HTL materials are advantageous for facile synthetic tunability, thus opening avenues to examine the relationship between band alignment and charge extraction at the HTL/perovskite interface.

Here, to correlate energy-level alignment and interfacial charge extraction at the perovskite/charge transport layer boundary in PVSCs, we fabricated and characterized fullerene/methylammonium lead triiodide ($MAPbI_3$) perovskite planar heterojunction solar cells comprising a series of three anionic poly(arylene vinylene)-based HTLs (Figure 1). Specifically, the HTLs were (1) poly(benzothiadiazole vinylene-*alt*-2,5-bis(4-sodium sulfonate)butoxy)-1,4-phenylenevinylene) ($PVBT\text{-}SO_3$); (2) poly(5,6-difluorobenzo[*c*][1,2,5]thiadiazole vinylene-*alt*-2,5-bis(4-sodium sulfonate)butoxy)-1,4-phenylenevinylene) ($PVF_2BT\text{-}SO_3$); and (3) poly(2,3,5,6-tetrafluorobenzene vinylene-*alt*-2,5-bis(4-sodium sulfonate)butoxy)-1,4-phenylenevinylene) ($PVF_4\text{-}SO_3$).[39,40] These polymers all contain identical sulfonate pendent groups and possess different arylene vinylene-based conjugated backbones, which tailor their HOMO energy levels. Using these polymers as HTLs at the interface between an $MAPbI_3$ active layer and indium tin oxide (ITO) electrode, the electronic structure at the contacting interface was varied to study the hole extraction process. The anionic pendent groups of the HTLs were found in perovskites with similar structures and morphologies, eliminating other variables that influence perovskite charge extraction and transport. Overall, tuning the energy levels of the perovskites and the HTLs dramatically improved hole extraction and increased the device efficiency by over 30%, consistent with time-resolved microwave conductivity (TRMC) measurements.

EXPERIMENTAL SECTION

Materials. C_{60}-ionene, $PVBT\text{-}SO_3$, $PVF_2BT\text{-}SO_3$, and $PVF_4\text{-}SO_3$ were prepared according to previously reported procedures.[39,41] Methylammonium iodide (MAI, >99.5%), PbI_2 (>99.99%) and $PC_{61}BM$ were purchased from Xi'an Polymer Light Technology Corp. γ-Butyrolactone (GBL, >99%) was purchased from TCI, dimethyl sulfoxide (DMSO, anhydrous, >99.7%) was obtained from Acros Organics, and chlorobenzene (anhydrous, >99.8%) was received from Sigma-Aldrich and used without further purification.

Fabrication of Perovskite Devices. ITO-coated glass substrates (1.5 × 1.5 cm^2, 15 Ω/sq), obtained from South China Science & Technology Ltd., were cleaned by sequential ultrasonic treatment in detergent, deionized water, acetone, and isopropyl alcohol, and then oven-dried at 60 °C to remove the residual isopropanol, followed by UV-ozone treatment for 15 min. $PVBT\text{-}SO_3$, $PVF_2BT\text{-}SO_3$, or $PVF_4\text{-}SO_3$ solution in deionized water was applied by spin-coating at 3500 rpm for 40 s onto precleaned ITO substrates. After spin-coating, the substrates were transferred into a N_2 (g)-filled glovebox. To synthesize $MAPbI_3$ perovskite films, the precursor solution was prepared by dissolving PbI_2 and MAI (1:1 molar ratio, 930 mg/mL in total) in a 3/7 (v/v) mixture of DMSO and GBL. This precursor solution was stirred at 60 °C for 4 h and then deposited onto the polymer-coated substrates with a two-step spin-coating procedure: (1) 1500 rpm for 20 s and (2) 4000 rpm for 60 s. Chlorobenzene (300 μL) was applied to the spinning substrate during the second spin-coating step at 40 s before the end of the procedure. The samples were then thermally annealed at 100 °C for 10 min inside the glovebox (N_2 (g) atmosphere, <0.1 ppm O_2, <0.1 ppm H_2O). A 60–70 nm $PC_{61}BM$ layer was cast onto the perovskite film from a chlorobenzene solution (20 mg/mL) inside the glovebox. Subsequently, C_{60}-ionene in trifluoroethanol (2 mg/mL) was spin-coated onto the $PC_{61}BM$ surface as an interlayer with a thickness of ∼10 nm. Finally, a Cu cathode (100 nm) was deposited onto the C_{60}-ionene layer under high vacuum (10^{-6} mbar) using a thermal evaporator and metal shadow mask to define an area of 0.04 cm^2 by the overlap of the ITO and the Cu cathode.

Device Characterization. *Current Density–Voltage (J–V).* The *J–V* characteristics of the devices were measured under simulated AM1.5G irradiation (100 mW/cm^2) using an EnliTech Class AAA Solar Simulator containing a Xe lamp equipped with an AM1.5G filter in the glovebox. The light intensity was adjusted with an NREL-calibrated Si solar cell with a KG-5 filter. Keithley 2400 was used as the source meter at a scanning rate of 100 mV/s (with a voltage step of 10 mV).

Time-Resolved Microwave Conductivity (TRMC). $MAPbI_3$ with or without the HTL was prepared in the same manner as the solar cells, without the electrode, and by replacing fluorine doped tin oxide (FTO)/glass with a quartz plate. The sample was set in a resonant cavity and subjected to continuous microwave exposure at ∼9.1 GHz. The excitation laser from an optical parametric oscillator (OPO, Continuum, Inc., Panther) seeded by the third harmonic generation

https://dx.doi.org/10.1021/acsami.0c18108
ACS Appl. Mater. Interfaces 2020, 12, 56068–56075

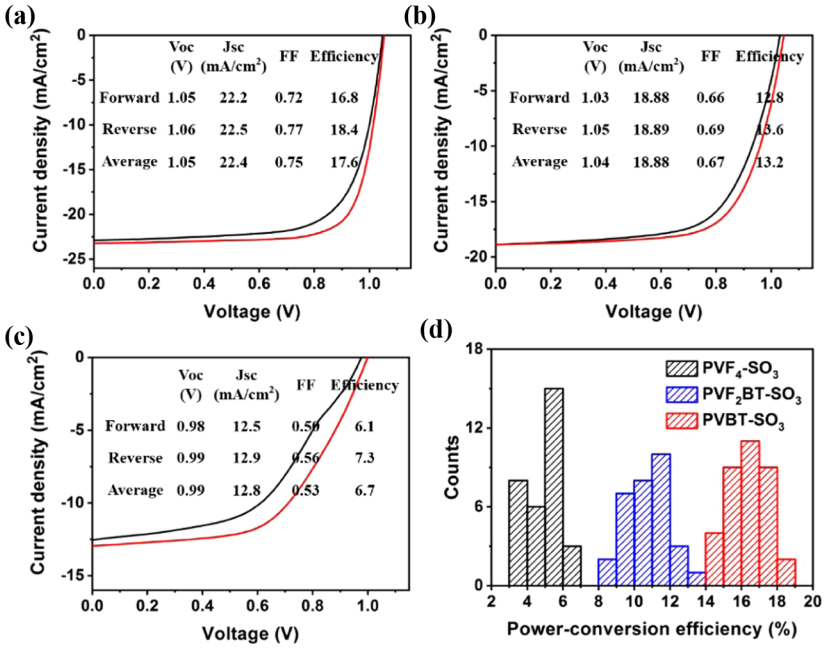

Figure 2. Representative $J-V$ curves of perovskite solar cells containing HTLs composed of (a) PVBT-SO_3, (b) PVF_2BT-SO_3, and (c) PVF_4-SO_3. (d) PCE histograms generated from ∼90 device measurements (∼30 devices were fabricated for each HTL composition).

of a Nd:YAG laser (Continuum, Inc., Surelite II, 5−8 ns pulse duration, 10 Hz) was set at 500 nm at an incident photon density (I_0) of 1.3×10^{11} photons cm^{-2} $pulse^{-1}$. The laser pulse was exposed from the HTL side, and the excitation wavelength was chosen to minimize laser absorption by the HTL. The low I_0 allows for a precise evaluation of η_{HT}, since $\phi\sum\mu_{max}$ lies in the flat region ($\phi \sim 1$), unaffected by a small change of I_0. The photoconductivity transient $\Delta\sigma$ is converted to the product of the quantum efficiency of charge carrier generation (ϕ) and the sum of charge carrier mobilities, $\sum\mu$ ($= \mu_+ + \mu_-$) by $\phi\sum\mu = \Delta\sigma\ (eI_0F_{light})^{-1}$, where e and F_{light} represent the unit charge of a single electron and a correction factor, respectively. The solar cells were kept at room temperature in air.

RESULTS AND DISCUSSION

Fullerene/perovskite planar heterojunction solar cells were fabricated containing a series of poly(arylene vinylene)-based anionic polyelectrolytes (Figure 1). Aqueous solutions of PVBT-SO_3, PVF_2BT-SO_3, and PVF_4-SO_3 were spin-coated separately onto ITO substrates, to serve as HTLs (Figure S1). The perovskite precursor solution (PbI_2 and MAI) was first spin-coated onto the HTL-coated substrates, followed by thermal annealing at 100 °C for 10 min to form the photoactive perovskite layer. As shown in Figure S2, uniform and continuous perovskite films appeared essentially identical irrespective of the polymers employed, which is consistent with the X-ray diffraction patterns (Figure S3), which showed similar perovskite order and orientation. $PC_{61}BM$ was deposited onto the perovskite layers to facilitate electron extraction from perovskite to ETL, followed by spin-coating a thin interfacial modification layer of C_{60}-ionene (Figure 1c).[41] Finally, copper (Cu) electrodes were deposited by thermal evaporation on the C_{60}-ionene layer. Figure 2 presents representative $J-V$ curves obtained for these devices, with the inset tables showing the corresponding device parameters. Devices with PVBT-SO_3 HTLs performed optimally, with a maximum PCE of 18.4%, V_{OC} of 1.06 V, J_{SC} of 22.5 mA/cm^2, and FF of 77%. PVF_2BT-SO_3 HTLs provided a moderate device performance, with a maximum PCE of 13.6%, mainly due to lower J_{SC} and FF values, while devices containing PVF_4-SO_3 HTLs were the least efficient of those studied, with PCE of 7.3%, V_{OC} of 1.00 V, J_{SC} of 13.0 mA/cm^2, and FF of 56%. Figure 2d shows the histogram of the average PCEs calculated from forward and reverse scans for all of the independent devices. Over 30% of the devices (11 devices) with PVBT-SO_3 HTLs exhibited efficiencies exceeding 17%, while the majority of devices with PVF_2BT-SO_3 or PVF_4-SO_3 HTLs gave efficiencies below 12 and 6%, respectively. As shown in Figure S4, EQE and the stabilized power output results are also consistent with the $J-V$ measurements, confirming the superior performance of PVBT-SO_3-based devices. As shown in Figure S5, surface energies were calculated to be 42.5 mN/m for PVBT-SO_3, 42.4 mN/m for PVF_2BT-SO_3, and 42.5 mN/m for PVF_4-SO_3 surfaces. Thus, since these polymer HTLs bear the same ionic pendent group and afford similar surface energies, the electronic structure associated with the conjugated backbone must be a critical determining factor for device efficiency.

Ultraviolet photoelectron spectroscopy (UPS) was used to characterize the intrinsic electronic characteristics in the polymer thin films and at the polymer−metal interface (Figure 3a,b). All of the polymer interlayers showed negligible influence on the work function of the metal electrode, as evidenced by the similar secondary electron cutoff in the high binding energy region of the spectra (Figure 3a, Table S1): The average secondary electron cutoff (E_{sec}) = 4.48, 4.54, and 4.60 eV for PVBT-SO_3, PVF_2BT-SO_3, and PVF_4-SO_3, respectively. The average HOMO onset was observed at 0.79, 0.86, and 1.06 eV from the Fermi levels for PVBT-SO_3, P4VF_2BT-SO_3, and PVF_4-SO_3, respectively (Figure 3b). Thus, the calculated average ionization potentials (IPs) of PVBT-SO_3, PVF_2BT-SO_3, and PVF_4-SO_3 from the UPS measurements are 5.27, 5.40, and 5.66 eV, respectively. We then performed photoelectron yield spectroscopy (PYS) to determine IPs of the polymer interlayers. As shown in Figure 3c, PVBT-SO_3, PVF_2BT-SO_3, and PVF_4-SO_3 gave IP values of

https://dx.doi.org/10.1021/acsami.0c18108
ACS Appl. Mater. Interfaces 2020, 12, 56068−56075

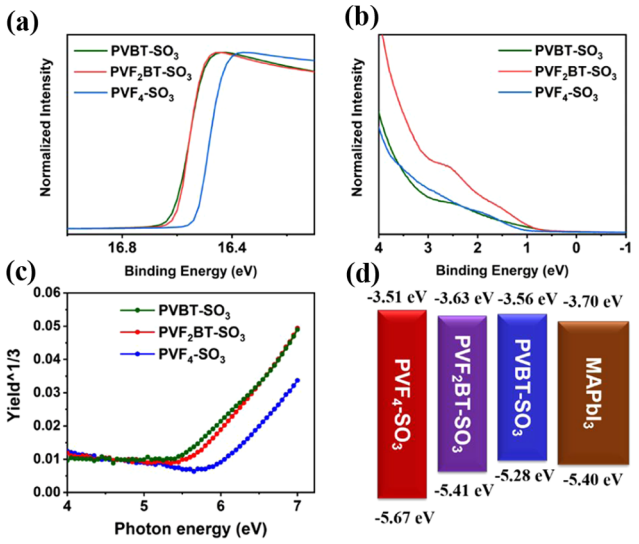

Figure 3. (a) E_{sec} and (b) HOMO onset of the UPS spectra; (c) photoelectron yield spectroscopy (PYS) characterizations of HTLs on metal substrates; and (d) energy-level diagram of HTLs and $MAPbI_3$ perovskite.

5.43, 5.53, and 5.83 eV, respectively, noting that the fluorinated polymer gave the largest IP value, in accordance with the electron-withdrawing characteristic of fluorine that induce a deeper HOMO energy level.[42] This is in close agreement with the values estimated by UPS. Thus, the energy-level diagram of perovskite and the HTLs can be illustrated as seen in Figure 3d.

Flash hyphen photolysis time-resolved microwave conductivity (TRMC) measurements were performed to study hole transporting process from the perovskite layer to the various HTLs. By comparing the $\phi\sum\mu$ transients (ϕ is the quantum efficiency of charge carrier generation and $\sum\mu$ is the sum of charge carrier mobilities) of perovskite/$PC_{61}BM$ and HTL/perovskite/$PC_{61}BM$ films, the hole transfer yield (η_{HT}) is evaluated by[43]

$$\eta_{HT} = \frac{\phi\sum\mu(t) - \phi\sum\mu_{HTL}(t)}{\phi\sum\mu(t)}$$

where $\phi\sum\mu(t)$ and $\phi\sum\mu_{HTL}(t)$ are the time-dependent $\phi\sum\mu$ without and with an HTL, respectively.

Figure 4a shows the $\phi\sum\mu(t)$ and $\phi\sum\mu_{HTL}(t)$ transients for the three polyelectrolyte HTLs, with $PVBT\text{-}SO_3$ showing the most rapid decay, followed by $PVF_2BT\text{-}SO_3$ and $PVF_4\text{-}SO_3$. The resultant η_{HT} values of the three HTLs, evaluated according to hole transfer yield, are shown in Figure 4b (η_{HT} = 1 signifies complete perovskite to HTL hole transfer). By analyzing the η_{HT} kinetics with a stretched exponential function ($\exp(-(kt)^{\beta})$), the four parameters of η_0 (initial hole transfer yield at the time resolution of TRMC), η_{sat} (saturated hole transfer yield at ~3 μs), k (hole transfer rate constant), and β (power factor) were obtained.

Table 1 summarizes hole transfer kinetics and indicates that devices containing $PVBT\text{-}SO_3$ show η_0 (0.63) nearly 2 times that of devices containing $PVF_2BT\text{-}SO_3$ (0.34) and $PVF_4\text{-}SO_3$ (0.32) HTLs. The $\eta_{HT}(t)$ values increase rapidly and reach η_{sat} = 0.80−0.91. The k values are 8.4×10^5 s^{-1} for $PVF_4\text{-}SO_3$, 1.6×10^6 s^{-1} for $PVF_2BT\text{-}SO_3$, and 7.5×10^6 s^{-1} for $PVBT\text{-}SO_3$, demonstrating the most efficient hole extraction by $PVBT\text{-}SO_3$. The $PVBT\text{-}SO_3$-based device showed the highest PCE (17.57%) among those analyzed ($PVF_2BT\text{-}SO_3$: 13.16% and $PVF_4\text{-}SO_3$: 6.69%), consistent with the hole transfer yield and the position of the HOMO energy level. Optimizing the energy-level alignment at the HTL/perovskite interface is

Table 1. Summary of Hole Transfer Kinetics

HTL	η_0	η_{sat}	k (s^{-1})	β
$PVF_4\text{-}SO_3$	0.32	0.80	8.4×10^5	1.00
$PVF_2BT\text{-}SO_3$	0.34	0.90	1.6×10^6	0.99
$PVBT\text{-}SO_3$	0.63	0.91	7.5×10^6	1.00

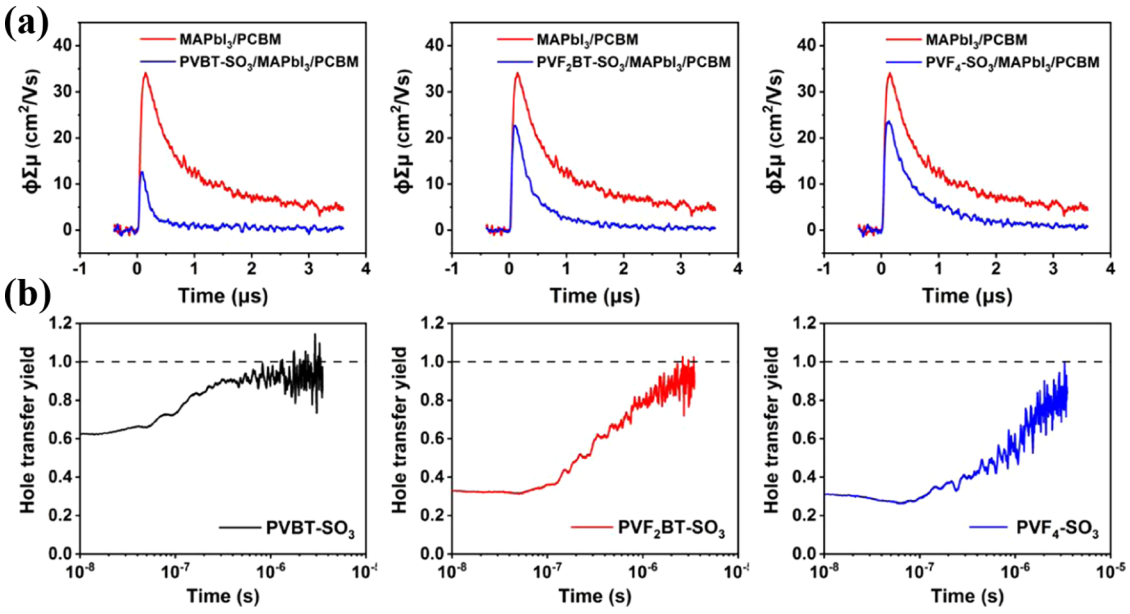

Figure 4. (a) $\phi\sum\mu$ transients and (b) semilogarithmic plot of hole transfer yield η_{HT} and time measured by TRMC (λ_{ex} = 500 nm, $I_0 = 1.3 \times 10^{11}$ photons/cm^2) for each device.

https://dx.doi.org/10.1021/acsami.0c18108
ACS Appl. Mater. Interfaces 2020, 12, 56068−56075

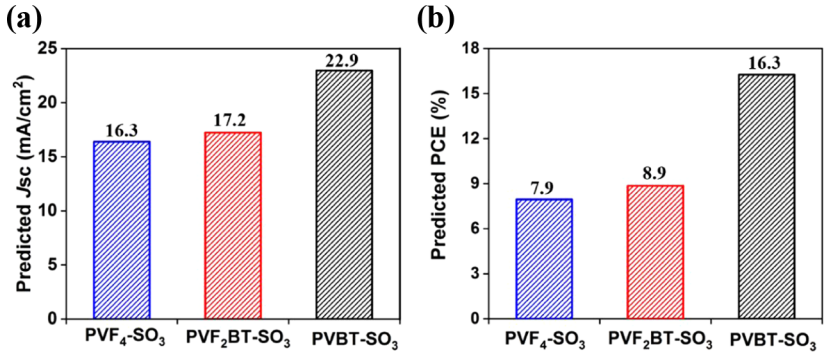

Figure 5. Predicted J_{SC} and PCE of perovskite-based solar cells with PVBT-SO_3, PVF_2BT-SO_3, and PVF_4-SO_3 as HTLs.

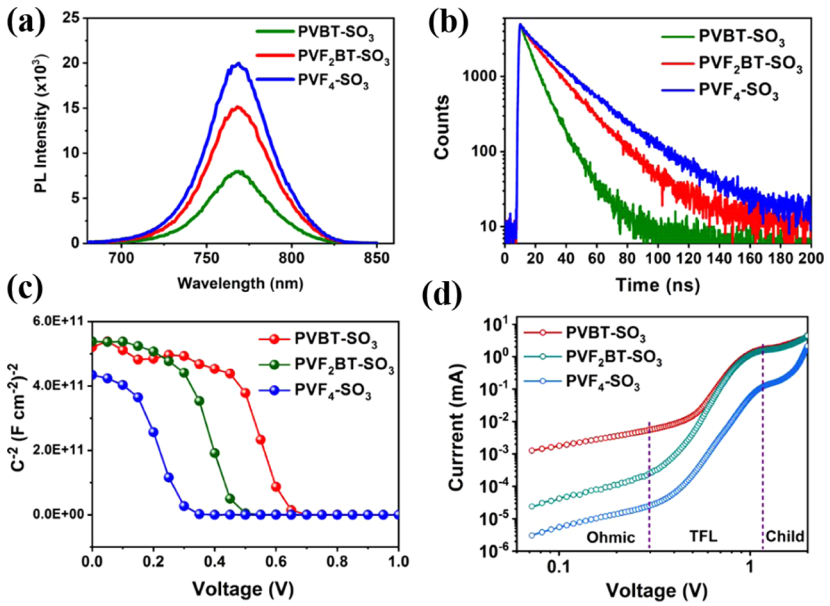

Figure 6. (a) PL spectra and (b) TRPL spectra for glass/HTL/perovskite samples; (c) Mott−Schottky plots of devices measured at 10 kHz probe frequency; and (d) SCLC measurements of the devices containing different HTLs (TFL = trap-filled regime).

clearly impactful for maximizing hole transfer kinetics and device performance.

TRMC evaluation was used to predict J_{SC} and PCE of the devices based on the observed correlation between TRMC results and device parameters of other HTL materials. In the previous study on the hole transfer dynamics evaluated by TRMC,[43] the logarithm of the product of initial hole transfer yield (η_0) and rate constant (k) was found to correlate with J_{SC} and PCE of $MAPbI_3$-based perovskite solar cell among various HTL materials. Using this indicator ($\ln(\eta_0 k)$), the J_{SC} and PCE of the perovskite solar cells were interpolated and predicted using three HTL materials from their TRMC results. The devices containing PVBT-SO_3 gave the best predicted performance with a J_{SC} of 22.9 mA/cm^2 and a PCE of 16.3%, while those containing PVF_2BT-SO_3 (J_{SC} = 17.9 mA/cm^2, PCE = 9.6%) and PVF_4-SO_3 (J_{SC} = 16.3 mA/cm^2, PCE = 7.9%) were much lower (Figure 5), in agreement with experimental results.

To investigate the hole extraction capability of the selected HTLs, steady-state photoluminescence (PL) and time-resolved photoluminescence (TRPL) decays at the peak emission of 405 nm were conducted for perovskite films on substrates coated with different HTLs. As shown in Figure 6a, the PL is strongly quenched in the presence of the PVBT-SO_3 HTL, indicative of efficient hole extraction. The TRPL decays are shown in Figure 6b. The single-exponential fits reveal PL decay constants of 23.40, 17.78, and 9.25 ns^{-1} for PVF_4-SO_3, PVF_2BT-SO_3, and PVBT-SO_3 layers, respectively. The results indicate that improved hole extraction and charge dissociation are achieved at the PVBT-SO_3/perovskite interface, in comparison to the other samples, and suggest that the band energy alignment at the HTL/perovskite interface is crucial for charge extraction, charge transfer and recombination. Thus, PVBT-SO_3 is the most efficient HTL having suitable energy-level alignment with the perovskites. We also performed PL and TRPL characterizations of perovskite films cast on ITO substrates (Figure S6). The data also support the most efficient hole extraction of PVBT-SO_3-based devices.

Figure 6c shows the Mott−Schottky plots of the three HTL-containing perovskite devices, which were recorded at a frequency of 10 kHz in the dark. Here, the Mott−Schottky equation was used to determine the flat-band potential of the three hole transport materials. The Mott−Schottky equation is given as[44]

$$\frac{1}{C_s^2} = \frac{2}{q\varepsilon\varepsilon_0 N}\left(V - V_{bi} - \frac{k_B T}{e}\right)$$

https://dx.doi.org/10.1021/acsami.0c18108
ACS Appl. Mater. Interfaces 2020, 12, 56068−56075

where C_s is the space charge capacitance per unit area; q, ε, and ε_0 are the electron charge, semiconductor dielectric constant, and permittivity of free space, respectively; and N, V, V_{bi}, k, and T are the carrier density, applied bias voltage, built-in potential, Boltzmann constant, and absolute temperature, respectively. From this equation, the built-in potential is determined from the intercept of the linear region, which represents the applied potential. Applying the experimental data to this equation, the flat-band potential of the three hole transport materials were calculated as 0.63 eV for PVBT-SO_3, 0.47 eV for PVF_2BT-SO_3, and 0.30 eV for PVF_4-SO_3. Standard p−n junction solar cell theory predicts that the V_{OC} of the device under illumination is limited by the V_{bi} of the junction.[45] Therefore, the value of V_{bi} is crucial for device performance and devices with the PVBT-SO_3 HTL possessed the largest V_{bi} and thus produced the highest V_{OC}.

In Figure 6d, the space charge limited current (SCLC) method is used to calculate the hole mobilities of the perovskite devices with the selected HTLs. The $J-V$ curve measured by the SCLC method is described in three regimes: a linear ohmic regime, a trap-filled regime beyond trap-filled limit voltage (V_{TFL}), and a trap-free SCLC regime. In the trap-free regime, the dark current shows a quadratic dependence ($k = 2$), known as the Child's law region according to the Mott−Gurney law. The SCLC mobility values are calculated from[46]

$$J_D = \frac{9\varepsilon\varepsilon_0\mu V_b^2}{8L^3}$$

where J_D is the current density, μ is the charge mobility, V_b is the applied voltage, ε_0 is the free space permittivity, ε is the relative dielectric constant of the perovskite, and L is the thickness of the perovskite layer. The relative dielectric constant ε of $MAPbI_3$ is 32 according to a previous study.[47] Curve fitting in the Child's law region provides the charge carrier mobility μ of the perovskite together with different HTLs as 0.36 $cm^2\ V^{-1}\ s^{-1}$ for PVBT-SO_3, 0.31 $cm^2\ V^{-1}\ s^{-1}$ for PVF_2BT-SO_3, and 0.03 $cm^2\ V^{-1}\ s^{-1}$ for PVF_4-SO_3. Thus, devices with a PVBT-SO_3/perovskite structure afforded the highest hole mobility. Since the conductivities of the three polymers are at the same level (Figure S7), the higher hole mobility of devices containing PVBT-SO_3 may be attributed to the better energy-level alignment between PVBT-SO_3 and perovskite.

CONCLUSIONS

The correlation between hole extraction and energy-level alignment of the HTL/perovskite interfacial contact region has been examined in detail. By varying the chemistry of the conjugated backbone of the HTL polymers, energy levels between perovskites and HTLs were better aligned, dramatically improving hole extraction efficiency and device performance. The hole transfer kinetics extracted from TRMC measurements show that an HTL with a suitable HOMO energy level is crucial for aligning the electronic structure and hole extraction efficiency at the HTL/perovskite interface. PL and electrical measurements further confirmed that improved alignment between the HTL and perovskite enables more efficient hole extraction and transport at the device interface. The experimental solar cell device performance was in good agreement with TRMC measurements and predictions, opening an avenue for evaluating structure−property relationships of interfacial layers through hole transfer kinetics analyses. These experimental results and theoretical calculations provide a comprehensive understanding of hole extraction and are anticipated to guide the design of next-generation hole transport materials for perovskite-based solar cell devices.

ASSOCIATED CONTENT

Supporting Information

The Supporting Information is available free of charge at https://pubs.acs.org/doi/10.1021/acsami.0c18108.

Detailed device characterizations, AFM images, SEM images, and XRD measurements (PDF)

AUTHOR INFORMATION

Corresponding Authors

Yao Liu − *Beijing Advanced Innovation Center for Soft Matter, Science and Engineering, State Key Laboratory of Chemical Resource Engineering, Beijing University of Chemical Technology, Beijing 100029, China;* orcid.org/0000-0001-8132-4987; Email: liuyao@mail.buct.edu.cn

Todd Emrick − *Polymer Science and Engineering Department, University of Massachusetts Amherst, Amherst, Massachusetts 01003, United States;* orcid.org/0000-0003-0460-1797; Email: tsemrick@mail.pse.umass.edu

Akinori Saeki − *Department of Applied Chemistry, Graduate School of Engineering, Osaka University, Osaka 565-0871, Japan;* orcid.org/0000-0001-7429-2200; Email: saeki@chem.eng.osaka-u.ac.jp

Thomas P. Russell − *Polymer Science and Engineering Department, University of Massachusetts Amherst, Amherst, Massachusetts 01003, United States;* orcid.org/0000-0001-6384-5826; Email: russell@mail.pse.umass.edu

Authors

Zhewei Zhang − *Beijing Advanced Innovation Center for Soft Matter, Science and Engineering, State Key Laboratory of Chemical Resource Engineering, Beijing University of Chemical Technology, Beijing 100029, China*

Madhu Sheri − *Polymer Science and Engineering Department, University of Massachusetts Amherst, Amherst, Massachusetts 01003, United States;* orcid.org/0000-0001-6850-5644

Zachariah A. Page − *Polymer Science and Engineering Department, University of Massachusetts Amherst, Amherst, Massachusetts 01003, United States;* orcid.org/0000-0002-1013-5422

Complete contact information is available at: https://pubs.acs.org/10.1021/acsami.0c18108

Notes

The authors declare no competing financial interest.

ACKNOWLEDGMENTS

Z.Z. and Y.L. acknowledge the support from the National Natural Science Foundation of China (NSFC) (21875018). T.P.R. was supported by the Office of Naval Research, Materials Division, under contract N00014-17-1-2241, and T.E. was supported by NSF-CHE 1904660.

REFERENCES

(1) Wang, P.; Zakeeruddin, S. M.; Comte, P.; Ivan, E.; Michael, G. Gelation of Ionic Liquid-Based Electrolytes with Silica Nanoparticles

for Quasi-Solid-State Dye-Sensitized Solar Cells. *J. Am. Chem. Soc.* **2003**, *125*, 1166−1167.
(2) Ito, S.; Zakeeruddin, S. M.; Humphry-Baker, R.; Liska, P.; Charvet, R.; Comte, P.; Nazeeruddin, M. K.; Péchy, P.; Takata, M.; Miura, H.; Uchida, S.; Grätzel, M. High-Efficiency Organic-Dye-Sensitized Solar Cells Controlled by Nanocrystalline-TiO_2 Electrode Thickness. *Adv. Mater.* **2006**, *18*, 1202−1205.
(3) Grätzel, M. The Light and Shade of Perovskite Solar Cells. *Nat. Mater.* **2014**, *13*, 838−842.
(4) Ansari, M. I. H.; Qurashi, A.; Nazeeruddin, M. K. Frontiers, Opportunities, and Challenges in Perovskite Solar Cells: A Critical Review. *J. Photochem. Photobiol., A* **2018**, *35*, 1−24.
(5) Liu, K.; Jiang, Y.; Jiang, Y.; Guo, Y.; Liu, Y.; Nakamura, E. Chemical Formation and Multiple Applications of Organic-Inorganic Hybrid Perovskite Materials. *J. Am. Chem. Soc.* **2019**, *141*, 1406−1414.
(6) Xing, G.; Mathews, N.; Sun, S.; Lim, S. S.; Lam, Y. M.; Gratzel, M.; Mhaisalkar, S.; Sum, T. C. Long-Range Balanced Electron-and Hole-Transport Lengths in Organic-Inorganic $CH_3NH_3PbI_3$. *Science* **2013**, *342*, 344−347.
(7) Chueh, C.-C.; Li, C.-Z.; Jen, A. K. Y. Recent Progress and Perspective in Solution-Processed Interfacial Materials for Efficient and Stable Polymer and Organometal Perovskite Solar Cells. *Energy Environ. Sci.* **2015**, *8*, 1160−1189.
(8) Meng, L.; You, J.; Guo, T. F.; Yang, Y. Recent Advances in the Inverted Planar Structure of Perovskite Solar Cells. *Acc. Chem. Res.* **2016**, *49*, 155−165.
(9) Djurišić, A. B.; Liu, F. Z.; Tam, H. W.; Wong, M. K.; Ng, A.; Surya, C.; Chen, W.; He, Z. B. Perovskite Solar Cells-An Overview of Critical Issues. *Prog. Quantum Electron.* **2017**, *53*, 1−37.
(10) Fakharuddin, A.; Schmidt-Mende, L.; Garcia-Belmonte, G.; Jose, R.; Mora-Sero, I. Interfaces in Perovskite Solar Cells. *Adv. Energy Mater.* **2017**, *7*, No. 1700623.
(11) Schulz, P.; Cahen, D.; Kahn, A. Halide Perovskites: Is It All about The Interfaces? *Chem. Rev.* **2019**, *119*, 3349−3417.
(12) Wang, S.; Sakurai, T.; Wen, W.; Qi, Y. Energy Level Alignment at Interfaces in Metal Halide Perovskite Solar Cells. *Adv. Mater. Interfaces* **2018**, *5*, No. 1800260.
(13) Han, T. H.; Tan, S.; Xue, J.; Meng, L.; Lee, J. W.; Yang, Y. Interface and Defect Engineering for Metal Halide Perovskite Optoelectronic Devices. *Adv. Mater.* **2019**, No. 1803515.
(14) Bai, Y.; Meng, X.; Yang, S. Interface Engineering for Highly Efficient and Stable Planar p-i-n Perovskite Solar Cells. *Adv. Energy Mater.* **2018**, *8*, No. 1701883.
(15) Pham, H. D.; Xianqiang, L.; Li, W.; Manzhos, S.; Kyaw, A. K. K.; Sonar, P. Organic Interfacial Materials for Perovskite-Based Optoelectronic Devices. *Energy Environ. Sci.* **2019**, *12*, 1177−1209.
(16) Rajagopal, A.; Yao, K.; Jen, A. K. Toward Perovskite Solar Cell Commercialization: A Perspective and Research Roadmap Based on Interfacial Engineering. *Adv. Mater.* **2018**, *30*, No. 1800455.
(17) Roose, B.; Wang, Q.; Abate, A. The Role of Charge Selective Contacts in Perovskite Solar Cell Stability. *Adv. Energy Mater.* **2018**, No. 1803140.
(18) Castro, E.; Murillo, J.; Fernandez-Delgado, O.; Echegoyen, L. Progress in Fullerene-Based Hybrid Perovskite Solar Cells. *J. Mater. Chem. C* **2018**, *6*, 2635−2651.
(19) Docampo, P.; Ball, J. M.; Darwich, M.; Eperon, G. E.; Snaith, H. J. Efficient Organometal Trihalide Perovskite Planar-Hetero-junction Solar Cells on Flexible Polymer Substrates. *Nat. Commun.* **2013**, *4*, No. 2761.
(20) Shao, Y.; Xiao, Z.; Bi, C.; Yuan, Y.; Huang, J. Origin and Elimination of Photocurrent Hysteresis by Fullerene Passivation in $CH_3NH_3PbI_3$ Planar Heterojunction Solar Cells. *Nat. Commun.* **2014**, *5*, No. 5784.
(21) Xu, J.; Buin, A.; Ip, A. H.; Li, W.; Voznyy, O.; Comin, R.; Yuan, M.; Jeon, S.; Ning, Z.; McDowell, J. J.; Kanjanaboos, P.; Sun, J. P.; Lan, X.; Quan, L. N.; Kim, D. H.; Hill, I. G.; Maksymovych, P.; Sargent, E. H. Perovskite-Fullerene Hybrid Materials Suppress Hysteresis in Planar Diodes. *Nat. Commun.* **2015**, *6*, No. 7081.
(22) De Bastiani, M.; Dell'Erba, G.; Gandini, M.; D'Innocenzo, V.; Neutzner, S.; Kandada, A. R. S.; Grancini, G.; Binda, M.; Prato, M.; Ball, J. M.; Caironi, M.; Petrozza, A. Ion Migration and The Role of Preconditioning Cycles in The Stabilization of The *J-V* Characteristics of Inverted Hybrid Perovskite Solar Cells. *Adv. Energy Mater.* **2016**, *6*, No. 1501453.
(23) Jeng, J. Y.; Chiang, Y. F.; Lee, M. H.; Peng, S. R.; Guo, T. F.; Chen, P.; Wen, T. C. $CH_3NH_3PbI_3$ Perovskite/Fullerene Planar-Heterojunction Hybrid Solar Cells. *Adv. Mater.* **2013**, *25*, 3727−3732.
(24) Kung, P. K.; Li, M. H.; Lin, P. Y.; Chiang, Y. H.; Chan, C. R.; Guo, T. F.; Chen, P. A Review of Inorganic Hole Transport Materials for Perovskite Solar Cells. *Adv. Mater. Interfaces* **2018**, *5*, No. 1800882.
(25) Park, I. J.; Park, M. A.; Kim, D. H.; Park, G. D.; Kim, B. J.; Son, H. J.; Ko, M. J.; Lee, D.-K.; Park, T.; Shin, H.; Park, N.-G.; Jung, H. S.; Kim, J. Y. New Hybrid Hole Extraction Layer of Perovskite Solar Cells with a Planar p-i-n Geometry. *J. Phys. Chem. C* **2015**, *119*, 27285−27290.
(26) Liu, Z.; Chang, J.; Lin, Z.; Zhou, L.; Yang, Z.; Chen, D.; Zhang, C.; Liu, S. F.; Hao, Y. High-Performance Planar Perovskite Solar Cells Using Low Temperature, Solution-Combustion-Based Nickel Oxide Hole Transporting Layer with Efficiency Exceeding 20%. *Adv. Energy Mater.* **2018**, *8*, No. 1703432.
(27) Lee, J. H.; Noh, Y. W.; Jin, I. S.; Park, S. H.; Jung, J. W. A Solution-Processed Cobalt-Doped Nickel Oxide for High Efficiency Inverted Type Perovskite Solar Cells. *J. Power Sources* **2019**, *412*, 425−432.
(28) Sun, W.; Peng, H.; Li, Y.; Yan, W.; Liu, Z.; Bian, Z.; Huang, C. Solution-Processed Copper Iodide as an Inexpensive and Effective Anode Buffer Layer for Polymer Solar Cells. *J. Phys. Chem. C* **2014**, *118*, 16806−16812.
(29) Jung, J. W.; Chueh, C.-C.; Jen, A. K. Y. High-Performance Semitransparent Perovskite Solar Cells with 10% Power Conversion Efficiency and 25% Average Visible Transmittance Based on Transparent CuSCN as The Hole-Transporting Material. *Adv. Energy Mater.* **2015**, *5*, No. 1500486.
(30) Zheng, X.; Lei, H.; Yang, G.; Ke, W.; Chen, Z.; Chen, C.; Ma, J.; Guo, Q.; Yao, F.; Zhang, Q.; Xu, H.; Fang, G. Enhancing Efficiency and Stability of Perovskite Solar Cells via a High Mobility P-type PbS Buffer Layer. *Nano Energy* **2017**, *38*, 1−11.
(31) Zuo, C.; Ding, L. Solution-Processed Cu_2O and CuO as Hole Transport Materials for Efficient Perovskite Solar Cells. *Small* **2015**, *11*, 5528−5532.
(32) Chen, L. C.; Chen, C. C.; Liang, K. C.; Chang, S. H.; Tseng, Z. L.; Yeh, S. C.; Chen, C. T.; Wu, W. T.; Wu, C. G. Nano-structured CuO-Cu_2O Complex Thin Film for Application in $CH_3NH_3PbI_3$ Perovskite Solar Cells. *Nanoscale Res. Lett.* **2016**, *11*, 402.
(33) Galatopoulos, F.; Savva, A.; Papadas, I. T.; Choulis, S. A. The Effect of Hole Transporting Layer in Charge Accumulation Properties of p-i-n Perovskite Solar Cells. *APL Mater.* **2017**, *5*, No. 076102.
(34) Zheng, X.; Hou, Y.; Bao, C.; Yin, J.; Yuan, F.; Huang, Z.; Song, K.; et al. Managing Grains and Interfaces via Ligand Anchoring Enables 22.3%-Efficiency Inverted Perovskite Solar Cells. *Nat. Energy* **2020**, *5*, 131−140.
(35) Lim, K.-G.; Ahn, S.; Kim, Y.-H.; Qi, Y.; Lee, T.-W. Universal Energy Level Tailoring of Self-Organized Hole Extraction Layers in Organic Solar Cells and Organic−Inorganic Hybrid Perovskite Solar Cells. *Energy Environ. Sci.* **2016**, *9*, 932−939.
(36) Zhang, J.; Chen, R.; Wu, Y.; Shang, M.; Zeng, Z.; Zhang, Y.; Zhu, Y.; Han, L. Extrinsic Movable Ions in $MAPbI_3$ Modulate Energy Band Alignment in Perovskite Solar Cells. *Adv. Energy Mater.* **2018**, *8*, No. 1701981.
(37) Yang, X.; Wang, H.; Cai, B.; Yu, Z.; Sun, L. Progress in Hole-Transporting Materials for Perovskite Solar Cells. *J. Energy Chem.* **2018**, *27*, 650−672.
(38) Zuo, C.; Ding, L. Modified PEDOT Layer Makes a 1.52 V V_{oc} for Perovskite/PCBM Solar Cells. *Adv. Energy Mater.* **2017**, *7*, No. 1601193.

https://dx.doi.org/10.1021/acsami.0c18108
ACS Appl. Mater. Interfaces 2020, 12, 56068−56075

(39) Page, Z. A.; Liu, Y.; Puodziukynaite, E.; Russell, T. P.; Emrick, T. Hydrophilic Conjugated Polymers Prepared by Aqueous Horner-Wadsworth-Emmons Coupling. *Macromolecules* **2016**, *49*, 2526−2532.
(40) Liu, Y.; Renna, L. A.; Page, Z. A.; Thompson, H. B.; Kim, P. Y.; Barnes, M. D.; Emrick, T.; Venkataraman, D.; Russell, T. P. A Polymer Hole Extraction Layer for Inverted Perovskite Solar Cells from Aqueous Solutions. *Adv. Energy Mater.* **2016**, *6*, No. 1600664.
(41) Liu, Y.; Sheri, M.; Cole, M. D.; Yu, D. M.; Emrick, T.; Russell, T. P. Transforming Ionene Polymers into Efficient Cathode Interlayers with Pendent Fullerenes. *Angew. Chem., Int. Ed.* **2019**, *58*, 5677−5681.
(42) Pelzer, K. M.; Cheng, L.; Curtiss, L. A. The Effects of Functional Groups in Redox-Active Organic Molecules: A High-Throughput Screening Approach. *J. Phys. Chem. C* **2017**, *121*, 237−245.
(43) Ishida, N.; Wakamiya, A.; Saeki, A. Quantifying Hole Transfer Yield from Perovskite to Polymer Layer: Statistical Correlation of Solar Cell Outputs with Kinetic and Energetic Properties. *ACS Photonics* **2016**, *3*, 1678−1688.
(44) Clifford, J. P.; Johnston, K. W.; Levina, L.; Sargent, E. H. Schottky Barriers to Colloidal Quantum Dot Films. *Appl. Phys. Lett.* **2007**, *91*, No. 253117.
(45) Straub, A.; Gebs, R.; Habenicht, H.; Trunk, S.; Bardos, R. A.; Sproul, A. B.; Aberle, A. G. Impedance Analysis: A Powerful Method for The Determination of The Doping Concentration and Built-in Potential of Nonideal Semiconductor p-n Diodes. *J. Appl. Phys.* **2005**, *97*, No. 083703.
(46) Peng, J.; Chen, Y.; Zheng, K.; Pullerits, T.; Liang, Z. Insights into Charge Carrier Dynamics in Organo-Metal Halide Perovskites: From Neat Films to Solar Cells. *Chem. Soc. Rev.* **2017**, *46*, 5714−5729.
(47) Dong, Q.; Fang, Y.; Shao, Y.; Mulligan, P.; Qiu, J.; Cao, L.; Huang, J. Electron-Hole Diffusion Lengths>175 mm in Solution-Grown CH3NH3PbI3 Single Crystals. *Science* **2015**, *347*, 967−970.

https://dx.doi.org/10.1021/acsami.0c18108
ACS Appl. Mater. Interfaces 2020, 12, 56068−56075